Assembly of Close-Packed Ferroelectric Polymer Nanowires via Interface-Epitaxy with ReS$_2$

*Dawei Li, Shuo Sun, Kun Wang, Zahra Ahmadi, Jeffrey E. Shield, Stephen Ducharme, and Xia Hong**

The flexible, transparent, and low-weight nature of ferroelectric polymers makes them promising for wearable electronic and optical applications. To reach the full potential of the polarization-enabled device functionalities, large-scale fabrication of polymer thin films with well-controlled polar directions is called for, which remains a central challenge. The widely exploited Langmuir–Blodgett, spin-coating, and electrospinning methods only yield polymorphous or polycrystalline films, where the net polarization is compromised. Here, an easily scalable approach is reported to achieve poly(vinylidene fluoride-trifluoroethylene) P(VDF-TrFE) thin films composed of close-packed crystalline nanowires via interface-epitaxy with 1T'-ReS$_2$. Upon controlled thermal treatment, uniform P(VDF-TrFE) films restructure into about 10 and 35 nm-wide (010)-oriented nanowires that are crystallographically aligned with the underlying ReS$_2$, as revealed by high-resolution transmission electron microscopy. Piezoresponse force microscopy studies confirm the out-of-plane polar axis of the nanowire films and reveal coercive voltages as low as 0.1 V. Reversing the polarization can induce a conductance switching ratio of >10^8 in bilayer ReS$_2$, over six orders of magnitude higher than that achieved by an untreated polymer gate. This study points to a cost-effective route to large-scale processing of high-performance ferroelectric polymer thin films for flexible energy-efficient nanoelectronics.

1. Introduction

The flexible, transparent, and low-weight nature of ferroelectric polymers makes them a promising material platform for developing wearable electronic and optical applications.[1–5] Leveraging their large, nanoscale controllable polarization, extensive research has been carried out on integrating poly(vinylidene fluoride-trifluoroethylene) P(VDF-TrFE) thin films with 2D van der Waals (vdW) materials for constructing a range of novel nanodevices,[6,7] including nonvolatile memories,[8–11] negative-capacitance field-effect transistors (FETs),[12,13] neuromorphic memristors,[14] and reconfigurable diodes.[10,11,15,16] One of the central challenges for technological implementation of these polarization-enabled device concepts is the lack of viable fabrication techniques for achieving large-scale crystalline polymer films with well-defined polarization direction. The widely exploited Langmuir–Blodgett (LB),[1,2,4,10,11] spin coating,[5,8,9,12–17] and electrospinning[18,19] methods only yield polymorphous or polycrystalline films with compromised net polarization, which significantly limit the device performance.

In this work, we report an easily scalable approach for fabricating highly ordered crystalline P(VDF-TrFE) nanowire (P-NW) films, which leverages the interfacial epitaxial relation with an anisotropic vdW material, 1T'-ReS$_2$. Upon controlled thermal treatment, uniform LB films self-assemble into close-packed NWs that are crystallographically aligned with the underlying ReS$_2$ with out-of-plane polar axis (**Figure 1**a). Compared with the pristine LB films, the P-NW films can lead to over six orders of magnitude higher ferroelectric field effect modulation in bilayer ReS$_2$ FET devices, and the coercive voltage can be as low as 0.1 V. Our approach offers a cost-effective strategy for achieving large-scale highly crystalline P(VDF-TrFE) thin films in the vdW heterostructure form, paving the path for their implementation in wearable energy-efficient nanoelectronics.

2. Results and Discussion

Using the horizontal LB deposition technique,[2] we deposited 1–9 monolayer (ML) P(VDF-TrFE) thin films on ReS$_2$ (Experimental Section). Figure 1b upper inset shows the atomic force microscopy (AFM) image of a 9 ML LB film prepared on a mechanically exfoliated single-layer (1L) ReS$_2$ flake on SiO$_2$ substrate (Figure S1, Supporting Information). After controlled thermal annealing, the initially smooth and uniform film reconstructs into well aligned, close-packed NWs with an average width of 35 nm (Figure 1b; Figure S2, Supporting Information), which are perpendicular to the Re chain

Prof. D. W. Li, Dr. S. Sun, K. Wang, Prof. S. Ducharme, Prof. X. Hong
Department of Physics and Astronomy & Nebraska Center for Materials and Nanoscience
University of Nebraska-Lincoln
Lincoln, Nebraska 68588-0299, USA
E-mail: xia.hong@unl.edu
Z. Ahmadi, Prof. J. E. Shield
Department of Mechanical and Materials Engineering
University of Nebraska-Lincoln
Lincoln, NE 68588-0526, USA

ADVANCED
SCIENCE NEWS
www.advancedsciencenews.com

ADVANCED
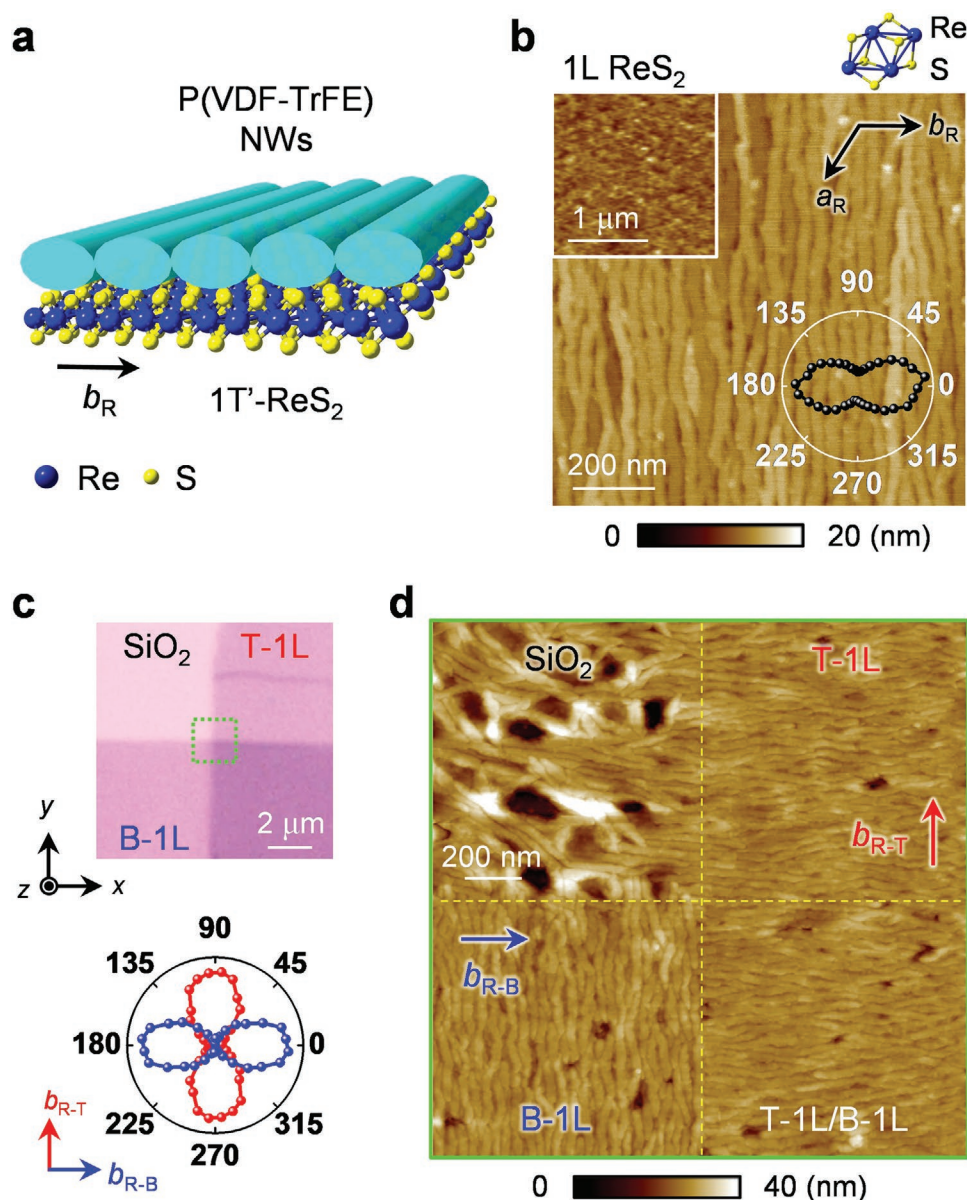**MATERIALS**
www.advmat.de

Figure 1. P-NW film on ReS₂. a) Sample schematic. b) AFM topography image of a P-NW film formed on 1L ReS₂. Upper inset: AFM image of the initial 9 ML LB film. Lower inset: polarization-resolved Raman signal of mode V of the 1L ReS₂. c) Optical image of two perpendicularly stacked 1L ReS₂ flakes (top), and the polar plots of parallel polarization-resolved Raman signal of mode V for the T-1L (red) and B-1L (blue) ReS₂ (bottom). d) AFM image of the boxed area in (c). The crystalline orientations of ReS₂ are labeled.

direction (b_R-axis). Figure 1c shows a sample prepared on two perpendicularly stacked 1L ReS₂. On the 1L ReS₂ regions, the NW orientations are perpendicular to the b_R-axis of the underlying ReS₂, which is in sharp contrast to the randomly oriented nanostructures formed on the SiO₂ substrate (Figure 1d).[20,21] Close to the edges of ReS₂, the NWs extend onto SiO₂, forming wire bundles that are perpendicular to each other. Interestingly, such a competing effect of NW orientation is not observed on the stacked bilayer ReS₂ region. Instead, the NW orientation is solely determined by the top layer (T-1L) ReS₂, forming a sharp interface with those on the bottom layer (B-1L). These results clearly point to an extremely short-ranged interfacial interaction between the P-NW and ReS₂. It is thus expected that the

thickness of ReS₂ is not a relevant factor for the NW formation. Indeed, we have achieved reliable fabrication of P-NWs on 1L, 2L, and few-layer ReS₂ flakes (Figure S3, Supporting Information), as well as bulk ReS₂ samples. **Figure 2**a shows the P-NW film prepared on a bulk ReS₂ single crystal, with the dimension approaching the centimeter scale, confirming the scalability of this fabrication approach.

To understand the role of the base layer in the P-NW formation, we prepared P(VDF-TrFE) samples on five other 2D vdW materials using identical fabrication methods (Figure S4, Supporting Information). The samples prepared on the isotropic 2H-MoS₂, graphene, and α-In₂Se₃ form randomly distributed rice-like nanograins, similar to previous reports on graphene.[9]
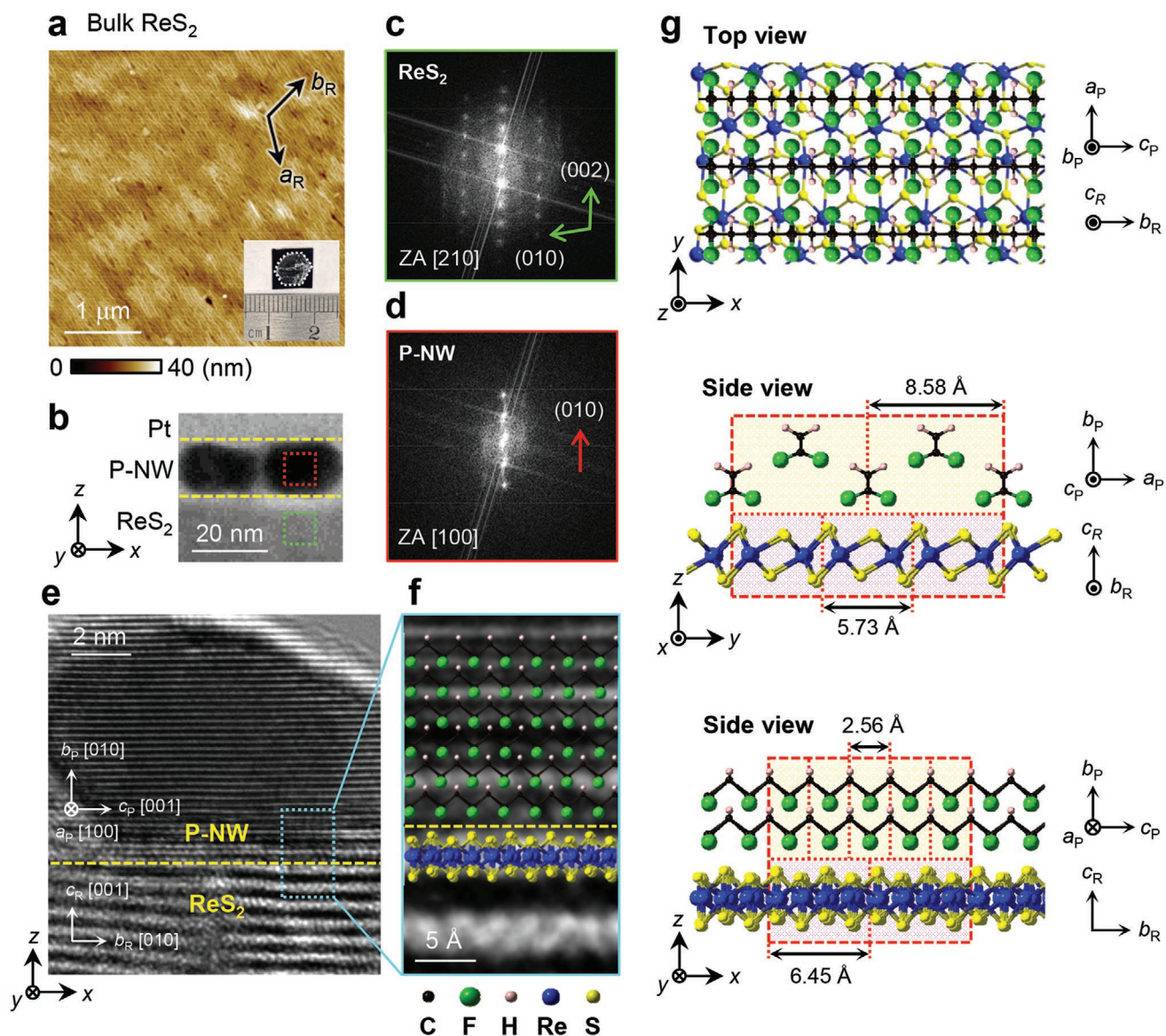
Figure 2. Structural properties of P-NW on ReS$_2$. a) AFM topography image of a P-NW film on bulk ReS$_2$. Lower inset: optical image of the sample laid on a SiO$_2$ substrate. The dotted lines outline the ReS$_2$ single crystal. b) Cross-sectional TEM image of a sample prepared on bulk ReS$_2$. c,d) Fast Fourier transform results for ReS$_2$ (c) and P-NW (d) taken from the boxed areas in (b). e) High-resolution TEM image of a P-NW on ReS$_2$. f) Expanded view of the boxed area in (e) superimposed with the atomic arrangements of ReS$_2$ and (010) P(VDF-TrFE). The interface between P(VDF-TrFE) and ReS$_2$ in (e) and (f) is marked by the dahsed lines. g) Schematic illustration of the epitaxial relation between P(VDF-TrFE) and ReS$_2$. The dashed lines mark the unit cells for P(VDF-TrFE) and ReS$_2$. The laboratory coordinate system and crystalline orientations of P(VDF-TrFE) and ReS$_2$ are labeled.

Surprisingly, samples prepared on anisotropic black phosphorus and TiS$_3$ also show isotropic nanograin distribution, indicating that the lattice anisotropy alone is not sufficient to align the P-NW assembly. To probe the details of the interfacial crystalline registration, we performed transmission electron microscopy (TEM) studies on a sample prepared on bulk ReS$_2$. Figure 2b shows the cross-sectional TEM image of two close-packed NWs. Fourier transform analysis of the image reveals clear diffraction spots for ReS$_2$ (Figure 2c) and P-NWs (Figure 2d), pointing to (010)-orientated P-NWs with high crystallinity. The high-resolution TEM image resolves the layered structure of one P-NW (Figure 2e) with interlayer spacing

of 2.48 ± 0.01 Å. This value agrees closely with half of the b_P-axis lattice parameter of orthorhombic P(VDF-TrFE) (70/30) ($b_P = 5.12$ Å),[22] confirming the (010)-orientation (Figure S5, Supporting Information). Mapping the atomic arrangements on the TEM image shows that the in-plane polymer chain (c_P-axis) is aligned with the Re-chain direction of ReS$_2$ (b_R-axis) (Figure 2f).

As illustrated in Figure 2g, in this configuration, there exists a clear epitaxial lattice relation between these two materials. In the y–z plane, the distance between five neighboring polymer chains ($2a_P \approx 17.16$ Å) matches well with three monomer distance of ReS$_2$ (≈ 17.19 Å). In the x–z plane, the extension of five

ADVANCED
SCIENCE NEWS
www.advancedsciencenews.com
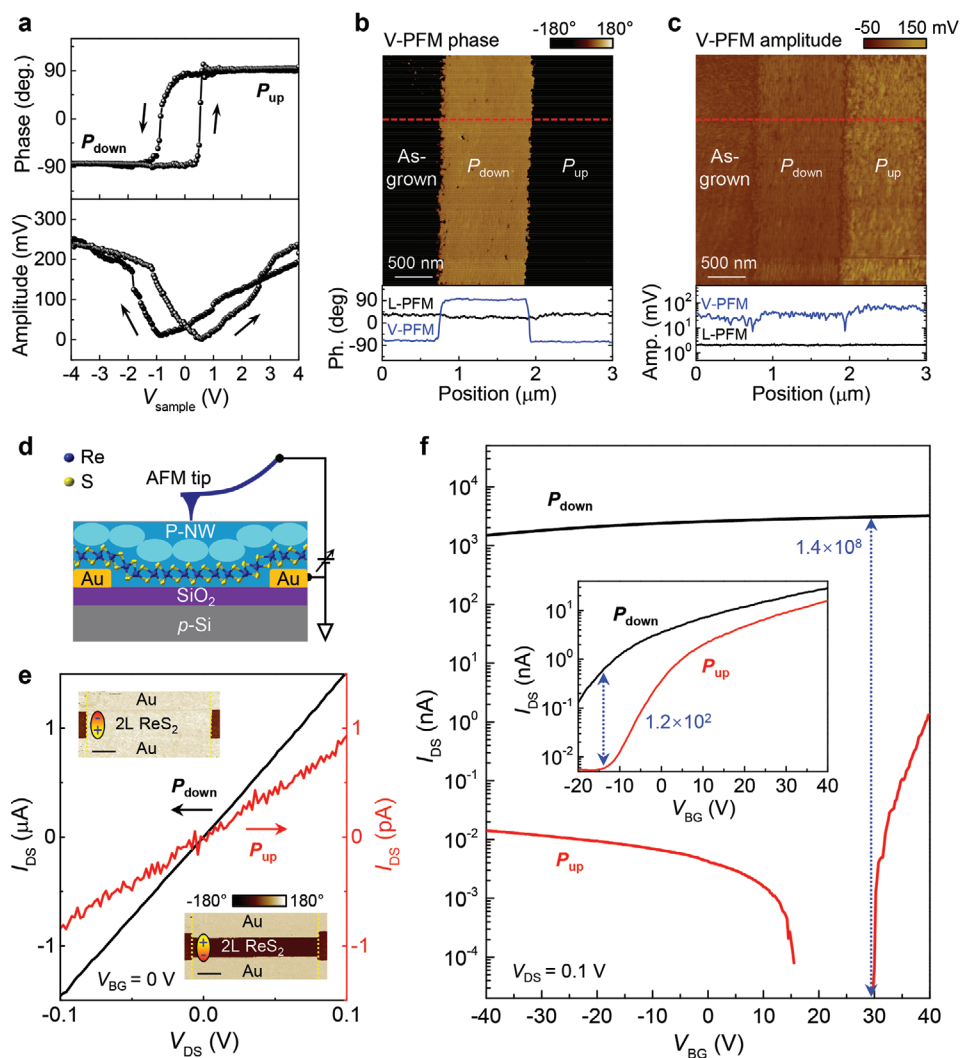
ADVANCED
MATERIALS
www.advmat.de

Figure 3. Characterizations of P-NWs and P-NW/ReS₂ FETs. a) V-PFM hystereses of phase (top) and amplitude (bottom) responses taken on a P-NW film prepared from a 9 ML LB film. b,c) PFM phase (b) and amplitude (c) images of a domain structure patterned on a P-NW film. The lower panels show the V-PFM and L-PFM signal profiles along the dashed lines. d–f) Characterizations of 2L ReS₂ FETs with SiO₂ back-gate and P(VDF-TrFE) top-gate at room-temperature. d) Device schematic. e) I_{DS} versus V_{DS} at V_{BG} = 0 V for the uniformly polarized P_{down} and P_{up} states of the P-NW top-layer, with the corresponding PFM phase images shown as insets. The scale bars are 2 µm. f) I_{DS} versus V_{BG} for the P_{down} and P_{up} states of the P-NW top-gate. Inset: I_{DS} versus V_{BG} of a 2L ReS₂ device top-gated by 9 ML untreated LB film for both polarization states.

P(VDF-TrFE) monomers ($5c_P \approx 12.8$ Å) closely match the distance between monomer units of ReS₂ ($2b_R \approx 12.9$ Å). As the interlayer interaction in orthorhombic P(VDF-TrFE) is also vdW type, we conclude that the close lattice match can enable the formation of an epitaxial vdW heterointerface between the P-NWs and ReS₂, with $b_P \parallel c_R$, $c_P \parallel b_R$, and $a_P \perp b_R$. The moderate in-plane tensile strain (0.2% along a_P and 0.8% along c_P) is also consistent with the slightly compressed interlayer spacing deduced from the TEM measurements. This scenario naturally explains why P(VDF-TrFE) on black phosphorus and TiS₃ only forms randomly distributed nanograins: the P-NW orientation on ReS₂ is guided by the epitaxial-type interfacial atomic registry, rather than merely the lattice symmetry. Unlike previous P-NW studies exploiting nanoimprinting[3,23] and AFM tip imposed mechanical annealing,[24] our approach leverages the crystalline interaction with the ReS₂ interface to guide

the NW self-assembly, which yields close-packed NWs forming large-scale continuous films.

We characterized the ferroelectric properties of the P-NW film via vertical and lateral piezoresponse force microscopy (PFM). **Figure 3**a shows the vertical PFM (V-PFM) switching hysteresis taken on a sample formed from 9 ML P(VDF-TrFE). The coercive voltages are approximately +0.6 and −0.8 V for the polarization up (P_{up}) and down (P_{down}) states, respectively. The corresponding coercive field (E_c) is about 0.05 V nm⁻¹ or less, which is significantly lower than the films prepared by the LB[25,26] method (0.1–1 V nm⁻¹) and becomes comparable with those of the oxide ferroelectrics.[27] Such low E_c can be attributed to the out-of-plane polar orientation of the P-NW films. Unlike the polycrystalline LB films, where the polarization points 30° away from the film normal,[28] the P-NWs crystalize along the polar axis (Figure 2f), requiring a significantly
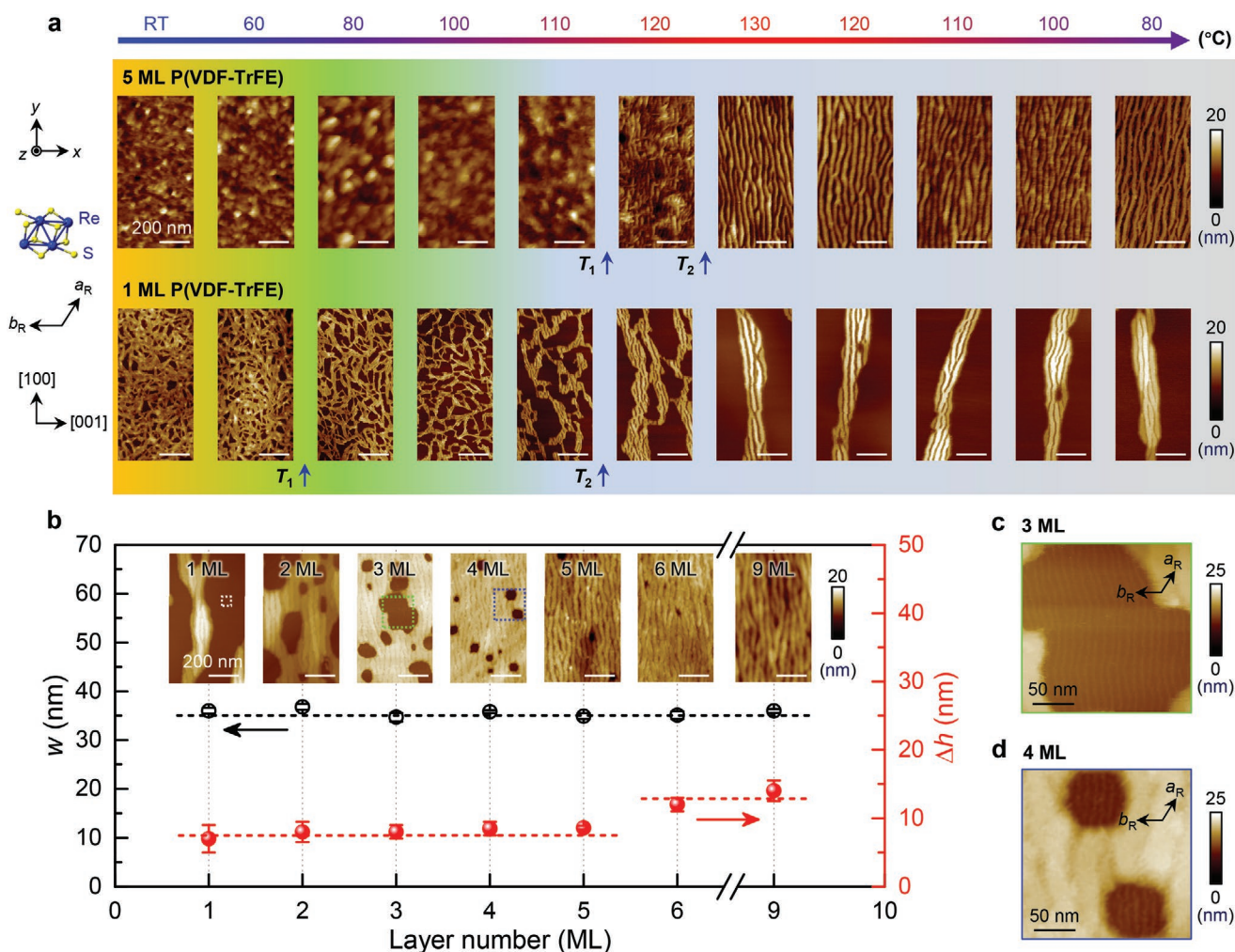
**ADVANCED
SCIENCE NEWS**
www.advancedsciencenews.com

**ADVANCED
MATERIALS**
www.advmat.de

Figure 4. Effects of temperature and LB film thickness. a) In situ AFM images of the surface morphology of 5 ML (top) and 1 ML (bottom) LB films on ReS_2 illustrating the P-NW formation process. The images do not correspond to the same sample area due to thermal drift of AFM. b) NW width w (left axis) and Δh (right axis) versus layer number of initial LB film, with AFM topography images of the corresponding P-NW films at room temperature (insets). The dashed lines serve as the guide to the eye. The crystalline orientations of ReS_2 are the same as in (a). c,d) Close-up AFM images taken on the (c) 3 ML and (d) 4 ML samples in the boxed areas in (b).

reduced switching field due to the polar anisotropy. Figure 3b,c shows the V-PFM images taken on the stripe P_{up} and P_{down} domains written on the sample. The as-grown state is close to the uniformly polarized P_{up} state, similar as the LB films.[29] The lateral PFM (L-PFM) signal on the same domain structure is close to the noise level for all three regions, with no appreciable dependence on the scanning angle (Figure S6, Supporting Information). This result indicates a lack of in-plane component of polarization, consistent with the out-of-plane polar axis of the (010) film. In contrast, annealed LB films typically crystallize in the (110) direction, which possesses intercorrelated in-plane and out-of-plane polarization.[25,30]

The out-of-plane polarization and small coercive voltage make the P-NW films an ideal choice as ferroelectric gate for FET devices (Figure 3d). Figure 3e shows the source–drain current–voltage relation ($I_{DS}-V_{DS}$) of a 2L ReS_2 device at zero back-gate bias ($V_{BG} = 0$ V), which corresponds to a channel conductivity switching ratio of 1.6×10^6 between the P_{up} and P_{down} states of the P-NW top-layer. Figure 3f compares the transfer

characteristics ($I_{DS}-V_{BG}$) of a 2L ReS_2 device for both polarizations of the P-NW top-gate. At $V_{BG} = 30$ V, the device shows a current switching ratio of 1.4×10^8. Even high switching ratio is expected at the gate range of $V_{BG} = 15$–30 V, where I_D is below the instrument resolution. In contrast, in a 2L ReS_2 device gated by untreated LB film, the highest current switching ratio is $\approx 1.2 \times 10^2$ (Figure 3f inset). The more than six orders of magnitude difference in the current switching ratio clearly illustrates the powerful gating capacity of highly crystalline P(VDF-TrFE) with out-of-plane polar axis.

To understand the formation mechanism of the P-NWs, we performed in situ AFM imaging on 5 and 1 ML P(VDF-TrFE) films on ReS_2 during the thermal treatment (**Figure 4**a). The 5 ML LB film does not show obvious change in morphology till a transition temperature $T_1 = 120$ °C, upon which the continuous film starts to transform into a texture composed of short NW segments. At this stage, there are short NWs lying along both x- and y-directions, which are parallel and perpendicular to the b_R axis of ReS_2, respectively. Further heating the sample to

ADVANCED
SCIENCE NEWS
www.advancedsciencenews.com

ADVANCED
MATERIALS
www.advmat.de

T_2 = 130 °C, the texture quickly evolves into well aligned NWs, where the x-oriented NWs disappear (or reorient) and y-oriented NWs merge into longer wires. The resulting P-NW film is continuous and stable upon cooling.

For the 1 ML P(VDF-TrFE), the initial LB film does not have a uniform surface coverage on ReS_2 at room temperature. Upon heating, randomly bundled fine NWs gradually emerge within the textures above a lower T_1 = 80 °C. These fine NWs start to reorient along y-axis at T_2 = 110 °C, with the neighboring ones merging into wider and longer NWs. The straightening and merging of NWs continue until 120 °C. Further heating the sample to 130 °C does not change the NW width, while the smaller patches congregate into large NW bundles. Similar to the 5 ML sample, the film maintains similar surface morphology during cooling. The NW formation, on the other hand, is highly sensitive to the thermal annealing temperature, and the well structured NWs would melt and break into isolated droplets when the sample is heated above 140 °C (Figure S7, Supporting Information).

As shown in Figure 4b insets, the morphology of the P-NW film evolves from scattered big islands of NW bundles to homogeneous films with fewer and fewer vacant areas with increasing layer number of the initial LB film. For all samples, however, we have full coverage of P-NWs over the entire sample surface. For the 6 ML and thicker samples, the final film is uniformly covered by wide NWs with no vacant spots over a large scale of area. The width (w) of the NWs ranges from 33 to 37 nm with no appreciate layer number dependence (Figure 4b). For samples thinner than 6 ML, the seemingly vacant regions are actually fully covered by fine NWs (Figure 4c,d), which are also aligned along the same orientation. The height difference (Δh) between the surfaces of the wide NW and fine NW regions is about 7–8 nm, also independent of the layer number. Taking into account the thickness of the fine NWs, i.e., about 7 nm (Figure 2b), we estimate the height of the wide NWs to be about 14–15 nm. We also measured the height of wide NWs directly on the 6 and 9 ML samples with respect to the pinholes, and obtained consistent results.

As shown in **Figure 5**a, the width of the fine NWs is about 10 nm. The PFM switching hystereses taken on the fine NW region reveal an ultralow coercive voltage of about ±0.1 V (Figure 5b), corresponding to an E_c below 0.02 V nm^{-1}. To assess the magnitude of polarization in the P-NWs, we monitored the in situ conductance change in 1L ReS_2 due to ferroelectric polarization doping of P(VDF-TrFE) during the P-NW formation process. As shown in Figure 5c, for a sample deposited with 9 ML of LB film, the conductance S of ReS_2 exhibits a sharp increase between T_1 and T_2, which is more than one order of magnitude higher than the thermal effect induced conductance variation in this ReS_2 sample before being coated with P(VDF-TrFE). This effect clearly illustrates the significant enhancement of polarization in the crystalline P-NWs compared with the polycrystalline LB film, as one would expect a lower polarization doping from the unstructured LB film with increasing temperature due to the pyroelectric effect. An even larger change is observed in the sample coated with 1 ML P(VDF-TrFE) (Figure 5d). The channel conduction is increased by over 10^3-fold between T_1 and T_2, which is more than two orders of magnitude higher than the change for ReS_2

in the pristine state. Upon cooling, the pristine ReS_2 samples recover the conductance S to the initial levels, as expected for a thermally activated behavior. For samples deposited with P(VDF-TrFE), in contrast, S only decreases moderately upon cooling, confirming that the P-NW film is stable. The fact that the conduction change in the ReS_2 sample deposited with 1 ML P(VDF-TrFE) is more than 10^2 times higher than the 9 ML sample demonstrates that the fine NWs not only preserve ferroelectricity, but likely possess even higher crystalline order with enhanced out-of-plane polar alignment, which is consistent with the lower E_c compared with the wide NWs.

The AFM and electrical characterizations reveal a two-stage P-NW formation process. The initial LB film is polymorphous, possessing both small crystallites and amorphous region (Figure 5e). As the sample is heated to T_1 (stage I), textures of short, fine P-NWs start to emerge, which are initially randomly oriented. The polymer chain is perpendicular to the NW orientation (Figure 2f). At the second transition temperature T_2 (stage II), the NWs gain sufficient thermal energy and become mobile on ReS_2. The interfacial interaction promotes the realignment of the NWs, with the adjacent NWs merging into longer fine (≈10 nm width) or wide (≈35 nm width) NWs. The merged NWs are mostly aligned along the direction perpendicular to b_R-axis of ReS_2. For the LB films thinner than 6 ML, the fine and wide P-NWs coexist to ensure a full surface coverage of P-NWs on ReS_2. For the 6 and 9 ML LB films, all fine NWs coalesce into wide NWs, resulting into close-packed uniform films, suggesting that the wide NW structure is more favorable when sufficient volume of the starting material is available.

Despite the starting LB film thickness, the final form of the P-NWs possesses similar width/height (Figure 4b), suggesting a self-termination process. This is similar to the thermal annealing effect on P(VDF-TrFE) LB films prepared on doped Si substrates below 4 ML thickness, where the initially uniform films segregate into isolated nanomesa structures with uniform heights of 9–10 nm.[31] Increasing the layer number only increases the density of the nanomesas, till they merge into a continuous film, without changing its height. The nanomesa formation process has been explained by considering the surface and elastic energies of the nanostructure and its interfacial interaction with the substrate.[32,33] These three energy contributions compete with each other: the surface and elastic energies prefer a uniform film distribution to maximize the surface to volume ratio, while the interaction between P(VDF-TrEF) and the substrate is repulsive in nature, driving the pattern coarsening to reduce the interface area. The net energy can be minimized at a critical structure height h_c regardless of the lateral dimension of the nanomesa. Similar scenario can be adopted to explain the P-NW formation on ReS_2. The key difference between the nanomesa structure and our system is the existence of an epitaxial relationship between P(VDF-TrFE) and ReS_2, which also lowers the interface energy. As shown in Figure 2g, the interfacial bonding density along the P-NW direction (y-axis) is much lower than the one along the b_R direction (x-axis). The epitaxial bonding energy prefers to have the polymer chain alinged along the b_R direction (x-axis), with the corresponding NW orientation perpendicular to b_R, while the repulsive interfacial interaction leads to a corrugated surface that is stablized at certian NW widths to optimize the
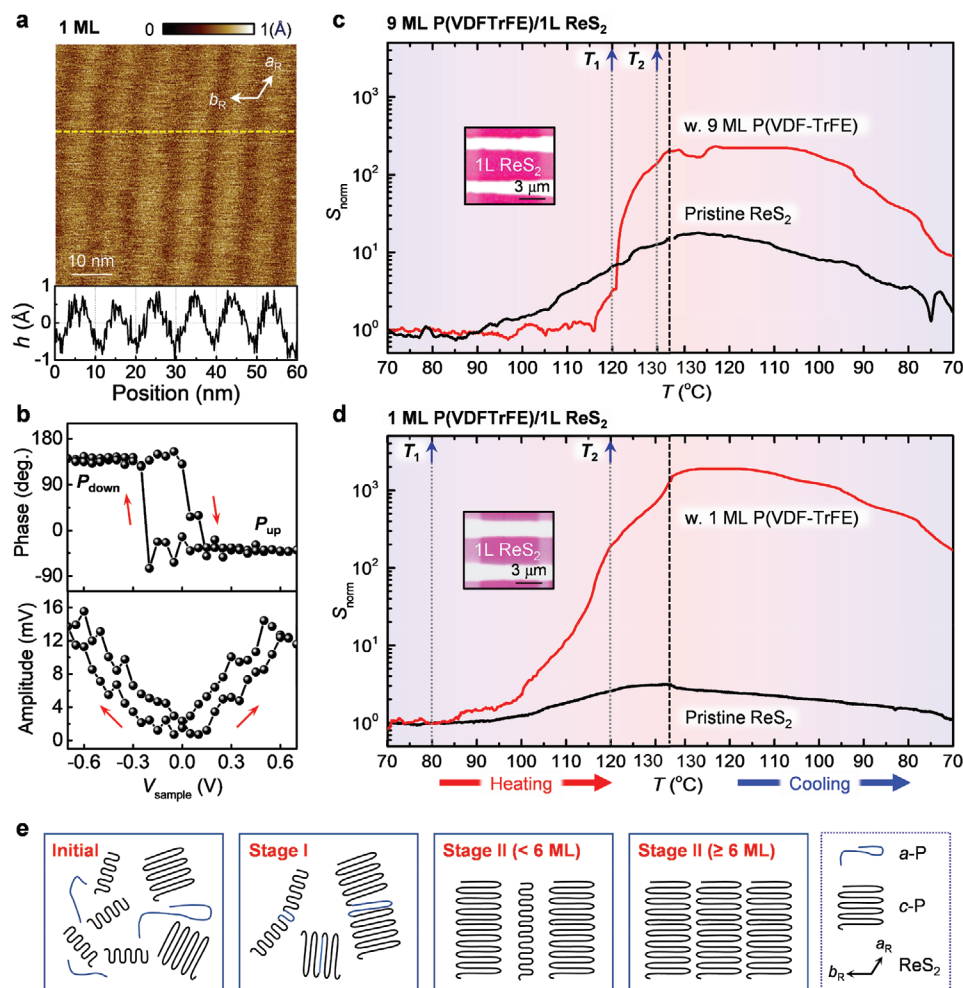
Figure 5. Characterizations of fine P-NWs and NW formation mechanism. a) Close-up AFM topography image taken on the 1 ML sample in the boxed area in Figure 4b, with the height profile along the dashed line (bottom). b) V-PFM hystereses of phase (top) and amplitude (bottom) responses taken on the fine NW film in (a). c) Conductance versus T for a 1L ReS$_2$ device in the pristine state (black) and with (red) 9 ML LB film deposited on top. The conductance is normalized to the value at 70 °C (S_{norm}). Inset: optical image of the ReS$_2$ device coated with 9 ML LB film. d) S_{norm} versus T for a 1L ReS$_2$ device in the pristine state (black) and with (red) 1 ML LB film deposited on top. Inset: optical image of the ReS$_2$ device coated with 1 ML LB film. The dotted lines in (c) and (d) mark T_1 and T_2 during heating. The dashed lines separate the heating and cooling regimes. e) Schematic illustration of a two-stage mechanism for P-NW formation facilitated by interfacial ReS$_2$. a-P: amorphous polymer chain. c-P: crystalline polymer chain.

contact area. In the direction perpendicular to Re-chain direction (y-axis), the surface/elastic energy dominates due to the low interfacial bonding density, leading to continuous long wires with large surface area. The net morphology is thus a result of the energy competition between the interfacial synergy and the self-energy of P(VDF-TrFE).

3. Conclusion

Unlike the polycrystalline or polymorphous P(VDF-TrEF) films, the close-packed P-NW films possess high crystallinity due to the interfacial epitaxial relation, enhanced out-of-plane polar alignment, and reduced coercive voltages that can be as low as 0.1 V, making them highly competitive for energy-efficient device applications. The large out-of-polarization of P-NW gate enables a remarkable nonvolatile current switching ratio

of exceeding 10^8 in bilayer ReS$_2$, which is among the highest values reported on P(VDF-TrFE)-gated 2D FETs.[6,7] As our approach is easily scalable for wafer-size production, it lays the important groundwork for implementing the ferroelectric polymer/2D vdW heterostructure for light-weight, low-power, wearable nanoelectronics and optoelectronics.

4. Experimental Section

Sample Preparation: Selected n-layer (nL, n = 1–10) ReS$_2$ flakes were mechanically exfoliated from bulk single crystals on elastomeric films (Gel-Film WF × 4 1.5 mil from Gel-Pak) and transferred on SiO$_2$ (290 nm)/ Si substrates using an all-dry transfer technique. The layer thickness was identified via the frequency difference Δ between the Mode I and Mode III in the Raman spectra (Figure S1, Supporting Information).[34]

P(VDF-TrFE) (70:30 mol%) copolymer films were deposited on ReS$_2$/ SiO$_2$ or ReS$_2$ single crystals by the horizontal LB technique from a

**ADVANCED
SCIENCE NEWS**

www.advancedsciencenews.com

**ADVANCED
MATERIALS**

www.advmat.de

water subphase. The P(VDF-TrFE) thin film was deposited one ML at a time. The thickness of 1 ML LB film is ≈2.0 nm. The as-grown P(VDF-TrFE) film is polycrystalline with low fraction of amorphous phase, with smooth morphology and no visible pinholes.[2] The samples were then annealed at 135 °C for 80 min to obtain the highly ordered P-NW films. The copolymer composition ratio of 70/30 VDF/TrFE was chosen because of its relatively high remnant polarization (≈10 μC cm^{-2}).[35,36]

TEM Studies: The TEM measurements were performed using a 200 kV TEM system (Tecnai Osiris Scanning, FEI) equipped with a field emission gun. The P-NW films are stable under this energy electron beam. The cross-sectioned TEM samples were prepared using the standard focused ion beam (FIB) lift-off technique via a FIB-SEM system (Thermo Science Helios NanoLab 660, FEI). A 5 nm thick Pt/Pd film was sputter-coated on top of the sample to prevent charge buildup during sample preparation. A 2 μm thick layer of Pt was then deposited to protect the sample during the ion milling. The cross-sectioned sample was mounted on a TEM copper grid and was further thinned to electron transparency.

Raman Characterization: Raman measurements were carried out using a micro-Raman system (Renishaw InVia plus, Renishaw). Raman spectra were collected with a 514.5 nm laser in reflection mode through a 50× objective lens with an accumulation time of 10 s. To avoid heating damage, the laser power was below 1 mW. For the polarized Raman measurements, the incident laser polarization was fixed with a linear polarizer, and the Raman signal was measured parallel to the laser polarization using a linear analyzer. The parallel polarization Raman signal was collected by rotating the sample from angle ϕ = 0°–360° in 10° steps.

Temperature-Dependent In Situ AFM Studies: The AFM and PFM measurements were conducted in a Bruker Multimode 8 AFM system. For the in situ thermal annealing measurements, the sample was placed on the AFM sample holder of the heating/cooling module. The temperature was controlled by the Bruker TAC Thermal Application Controller system. The sample was slowly heated to progressively higher temperatures. Before imaging, the sample was held for 10 min at the target temperature after the temperature was stabilized. The in situ topography scanning was conducted in tapping mode with silicon nitride AFM probes (Bruker SCANASYST-AIR, spring constant k of 0.2–0.8 N m^{-1}, resonant frequency f_o of 45–95 kHz). Due to thermal drift, the same area was not tracked. This will not affect the analysis since the sample is uniform on the large scale.

PFM Studies: The vertical PFM measurements were performed in contact mode with conductive PtIr-coated AFM probes (Bruker SCM-PIC-V2, spring constant k of 0.03–0.2 N m^{-1}, resonant frequency f_o of 4–10 kHz). The lateral PFM (L-PFM) measurements were performed with conductive PtIr-coated AFM probes (NanoSensors PPP-EFM, spring constant k of 0.5–9.5 N m^{-1}, resonant frequency f_o of 45–115 kHz). The scanning direction was perpendicular to the cantilever axis. The scanning-angle-dependent L-PFM signal was collected by rotating the sample from 0° to 180° in 15° steps. The noise floor for L-PFM is calibrated using the uniformly polarized domain and domain wall written on high quality epitaxial (001) PbZr$_{0.2}$Ti$_{0.8}$O$_3$ thin films (Figure S6, Supporting Information).[37]

FET Device Fabrication and Characterization: Cr/Au (5/25nm) electrodes were pre-patterned on SiO$_2$ (290nm)/ Si substrates in the two-point geometry using photolithography. Selected ReS$_2$ flakes were transferred on the electrodes, forming FET devices. P(VDF-TrFE) thin films were then deposited on the ReS$_2$ devices by the horizontal LB deposition technique. All electrical measurements were carried out using semiconductor parameter analyzer (Keysight 1500A) in ambient conditions.

Supporting Information

Supporting Information is available from the Wiley Online Library or from the author.

Conflict of Interest

The authors declare no conflict of interest.

Author Contributions

D.L. and S.S. contributed equally to this work. X.H. and D.L. conceived the project and designed the experiments. X.H. supervised the project. D.L. prepared the ReS$_2$ samples and devices, and carried out Raman and AFM characterizations. S.S. and S.D. prepared the P(DVF-TrFE) LB films. Z.A. and J.S. performed the TEM studies. D.L. and K.W. carried out the PFM studies. D.L. and S.S. prepared the P-NW films and carried out the electrical measurements. D.L. and X.H. wrote the manuscript. All authors discussed the results and contributed to the manuscript preparation.

Data Availability Statement

The data that support the findings of this study are available from the corresponding author upon reasonable request.

[1] A. V. Bune, V. M. Fridkin, S. Ducharme, L. M. Blinov, S. P. Palto, A. V. Sorokin, S. G. Yudin, A. Zlatkin, *Nature* **1998**, *391*, 874.

[2] S. Ducharme, S. Palto, V. M. Fridkin, in *Handbook of Thin Films*, Vol. *3*, (Ed: H. Singh Nalwa), Academic Press, Burlington, MA, USA **2002**, p. 545.

[3] Z. Hu, M. Tian, B. Nysten, A. M. Jonas, *Nat. Mater.* **2009**, *8*, 62.

[4] Y. Yuan, T. J. Reece, P. Sharma, S. Poddar, S. Ducharme, A. Gruverman, Y. Yang, J. Huang, *Nat. Mater.* **2011**, *10*, 296.

[5] M. Li, H. J. Wondergem, M.-J. Spijkman, K. Asadi, I. Katsouras, P. W. Blom, D. M. De Leeuw, *Nat. Mater.* **2013**, *12*, 433.

[6] X. Hong, *J. Phys.: Condens. Matter* **2016**, *28*, 103003.

[7] H. Ryu, K. Xu, D. Li, X. Hong, W. Zhu, *Appl. Phys. Lett.* **2020**, *117*, 080503.

[8] Y. T. Lee, H. Kwon, J. S. Kim, H.-H. Kim, Y. J. Lee, J. A. Lim, Y.-W. Song, Y. Yi, W.-K. Choi, D. K. Hwang, *ACS Nano* **2015**, *9*, 10394.

[9] K. L. Kim, W. Lee, S. K. Hwang, S. H. Joo, S. M. Cho, G. Song, S. H. Cho, B. Jeong, I. Hwang, J.-H. Ahn, *Nano Lett.* **2016**, *16*, 334.

[10] Z. Xiao, J. Song, D. K. Ferry, S. Ducharme, X. Hong, *Phys. Rev. Lett.* **2017**, *118*, 236801.

[11] D. Li, Z. Xiao, S. Mu, F. Wang, Y. Liu, J. Song, X. Huang, L. Jiang, J. Xiao, L. Liu, S. Ducharme, B. Cui, X. Hong, L. Jiang, J.-F. Silvain, Y. Lu, *Nano Lett.* **2018**, *18*, 2021.

[12] X. Wang, Y. Chen, G. Wu, D. Li, L. Tu, S. Sun, H. Shen, T. Lin, Y. Xiao, M. Tang, W. Hu, L. Liao, P. Zhou, J. Sun, X. Meng, J. Chu, J. Wang, *npj 2D Mater. Appl.* **2017**, *1*, 38.

[13] X. Liu, R. Liang, G. Gao, C. Pan, C. Jiang, Q. Xu, J. Luo, X. Zou, Z. Yang, L. Liao, *Adv. Mater.* **2018**, *30*, 1800932.

[14] Y. Chen, Y. Zhou, F. Zhuge, B. Tian, M. Yan, Y. Li, Y. He, X. S. Miao, *npj 2D Mater. Appl.* **2019**, *3*, 31.

[15] L. Lv, F. Zhuge, F. Xie, X. Xiong, Q. Zhang, N. Zhang, Y. Huang, T. Zhai, *Nat. Commun.* **2019**, *10*, 3331.

[16] G. Wu, B. Tian, L. Liu, W. Lv, S. Wu, X. Wang, Y. Chen, J. Li, Z. Wang, S. Wu, H. Shen, T. Lin, P. Zhou, Q. Liu, C. Duan, S. Zhang, X. Meng, S. Wu, W. Hu, X. Wang, J. Chu, J. Wang, *Nat. Electron.* **2020**, *3*, 43.

[17] M. Benz, W. B. Euler, O. J. Gregory, *Macromolecules* **2002**, *35*, 2682.

[18] J. Andrew, D. Clarke, *Langmuir* **2008**, *24*, 670.

[19] S.-H. Park, H. B. Lee, S. M. Yeon, J. Park, N. K. Lee, *ACS Appl. Mater. Interfaces* **2016**, *8*, 24773.

[20] T. Fukuma, K. Kobayashi, T. Horiuchi, H. Yamada, K. Matsushige, *Jpn. J. Appl. Phys.* **2000**, *39*, 3830.

[21] P. Sharma, T. Reece, D. Wu, V. M. Fridkin, S. Ducharme, A. Gruverman, *J. Phys.: Condens. Matter* **2009**, *21*, 485902.

[22] E. Bellet-Amalric, J. Legrand, *Eur. Phys. J. B* **1998**, *3*, 225.

[23] J. Song, H. Lu, S. Li, L. Tan, A. Gruverman, S. Ducharme, *Nanotechnology* **2016**, *27*, 015302.

[24] Y.-Y. Choi, P. Sharma, C. Phatak, D. J. Gosztola, Y. Liu, J. Lee, B. Lee, J. Li, A. Gruverman, S. Ducharme, S. Hong, *ACS Nano* **2015**, *9*, 1809.

[25] Z. Xiao, S. Poddar, S. Ducharme, X. Hong, *Appl. Phys. Lett.* **2013**, *103*, 112903.

[26] S. Ducharme, V. M. Fridkin, A. V. Bune, S. Palto, L. Blinov, N. Petukhova, S. Yudin, *Phys. Rev. Lett.* **2000**, *84*, 175.

[27] X. Chen, X. Zhang, M. A. Koten, H. Chen, Z. Xiao, L. Zhang, J. E. Shield, P. A. Dowben, X. Hong, *Adv. Mater.* **2017**, *29*, 1701385.

[28] H. Ohigashi, K. Omote, T. Gomyo, *Appl. Phys. Lett.* **1995**, *66*, 3281.

[29] L. Blinov, V. Fridkin, S. Palto, A. Sorokin, S. Yudin, *Thin Solid Films* **1996**, *284*, 474.

[30] P. Sharma, D. Wu, S. Poddar, T. J. Reece, S. Ducharme, A. Gruverman, *J. Appl. Phys.* **2011**, *110*, 052010.

[31] M. Bai, S. Ducharme, *Appl. Phys. Lett.* **2004**, *85*, 3528.

[32] J. Li, Y. Luo, M. Bai, S. Ducharme, *Appl. Phys. Lett.* **2005**, *87*, 213116.

[33] J. Li, Y. Luo, M. Bai, S. Ducharme, *J. Mech. Phys. Solids* **2006**, *54*, 2162.

[34] D. A. Chenet, O. B. Aslan, P. Y. Huang, C. Fan, A. M. van der Zande, T. F. Heinz, J. C. Hone, *Nano Lett.* **2015**, *15*, 5667.

[35] T. Furukawa, *Phase Transitions: Multinatl. J.* **1989**, *18*, 143.

[36] S. M. Nakhmanson, M. B. Nardelli, J. Bernholc, *Phys. Rev. Lett.* **2004**, *92*, 115504.

[37] D. Li, X. Huang, Z. Xiao, H. Chen, L. Zhang, Y. Hao, J. Song, D.-F. Shao, E. Y. Tsymbal, Y. Lu, X. Hong, *Nat. Comm.* **2020**, *11*, 1422.